Chinese Chemical Letters 33 (2022) 3961–3967

Contents lists available at ScienceDirect

Chinese Chemical Letters

journal homepage: www.elsevier.com/locate/cclet

Hierarchical porous carbon derived from coal-based carbon foam for high-performance supercapacitors

Nuannuan Yang[a,b], Lei Ji[c], Haichao Fu[a,b], Yanfeng Shen[a,b], Meijun Wang[a,b,**], Jinghai Liu[c,*], Liping Chang[a,b], Yongkang Lv[a,b]

[a] State Key Laboratory of Clean and Efficient Coal Utilization, Taiyuan University of Technology, Taiyuan 030024, China
[b] Key Laboratory of Coal Science and Technology, Ministry of Education and Shanxi Province, Taiyuan University of Technology, Taiyuan 030024, China
[c] Inner Mongolia Key Laboratory of Carbon Nanomaterials, Nano Innovation Institute (NII), College of Chemistry and Materials Science, Inner Mongolia Minzu University, Tongliao 028000, China

ARTICLE INFO

Article history:
Received 4 January 2022
Revised 20 February 2022
Accepted 10 March 2022
Available online 13 March 2022

Keywords:
Bituminous coal
Three-dimensional structure
KOH activation
Hierarchical porous carbon
Supercapacitor

ABSTRACT

Hierarchical porous carbon (HPC) from bituminous coal was designed and synthesized through pyrolysis foaming and KOH activation. The obtained HPC (NCF-KOH) were characterized by a high specific surface area (S_{BET}) of 3472.41 m^2/g, appropriate mesopores with V_{mes}/V_{total} of 57%, and a proper amount of surface oxygen content (10.03%). This NCF-KOH exhibited a high specific capacitance of 487 F/g at 1.0 A/g and a rate capability of 400 F/g at 50 A/g based on the three-electrode configuration. As an electrode for a symmetric capacitor, a specific capacitance of 299 F/g at 0.5 A/g was exhibited, and the specific capacitance retained 96% of the initial capacity at 5 A/g after 10,000 cycles. Furthermore, under the power density of 249.6 W/kg in 6 mol/L KOH, a high energy density of 10.34 Wh/kg was obtained. The excellent charge storage capability benefited from its interconnected hierarchical pore structure with high accessible surface area and the suitable amount of oxygen-containing functional groups. Thus, an effective strategy to synthesize HPC for high-performance supercapacitors serves as a promising way of converting coal into advanced carbon materials.

© 2022 Published by Elsevier B.V. on behalf of Chinese Chemical Society and Institute of Materia Medica, Chinese Academy of Medical Sciences.

Supercapacitors, a representative high-performance energy storage and conversion device, play a vital role in electrochemical energy storage systems because of their ultra-high cycle life and superior power density [1–4]. In accordance with the charge storage mechanism, supercapacitors are primarily composed of pseudo-capacitors and electric double-layer capacitors (EDLCs) [5–8]. EDLCs have aroused public attention for their simple structure, fast charge-discharge rates, superior cycle life, as well as stable properties. However, its relatively low specific capacitance and energy density limit their applications [9,10]. Thus, on the premise of ensuring the long cycle life and high power density, it is of critical importance to improve the specific capacitance and energy density of EDLCs. Carbon materials with high chemical stability, high conductivity, and high specific surface area (S_{BET}), are considered as superior candidate electrode materials for EDLCs [1,5]. Towards this aim, porous carbon (PC) can significantly improve the capacitance and energy density of supercapacitors due to the high S_{BET}, and the synergistic enhancement effects of multiscale pores [11,12]. Micropores (<2 nm) are capable of providing more active sites, contributing to the enhancement of energy storage capacity and increasing energy density. Mesopores (2–50 nm) can give ion channels, facilitating the ion diffusion and transport of electrolytes. Moreover, macropores (>50 nm) act as ion buffer reservoirs to shorten ion diffusion distance [13–16].

Coal has been extensively employed to prepare PC since coal resources are abundant, low in price and high in carbon content [17]. In addition, its macromolecules largely consist of aromatic ring structures, thus enhancing the conductivity of carbon materials [12,18,19]. At present, the preparation of PC with coal as a carbon source has primarily adopted the chemical activation method through direct mechanical mixing or impregnation of coal and activators [20–23]. The major pore-creating mechanism consists of coal undergoing oxidation–reduction reactions as impacted by the action of the activator (*e.g.*, KOH, $ZnCl_2$ and H_3PO_4) to facilitate the formation of a porous structure, and after the activators etch the coal particles based on an outside-in procedure, deep and branched pore structure are formed [12,23,24]. Specifically, with KOH as the activator, the synthesized PC with high S_{BET}

* Corresponding author.
** Corresponding author at: State Key Laboratory of Clean and Efficient Coal Utilization, Taiyuan University of Technology, Taiyuan 030024, China.
E-mail addresses: wangmeijun@tyut.edu.cn (M. Wang), jhliu2008@sinano.ac.cn (J. Liu).

https://doi.org/10.1016/j.cclet.2022.03.037
1001-8417/© 2022 Published by Elsevier B.V. on behalf of Chinese Chemical Society and Institute of Materia Medica, Chinese Academy of Medical Sciences.

mainly composed of micropores, exhibited optimal performance [25]. Kierzek *et al.* prepared microporous PC with a large S_{BET} of 3150 m^2/g, a pore volume of 1.61 cm^3/g, and a wide pore size distribution using highly volatile bituminous coal as the precursor based on KOH activation [26]. The synthesized PC as electrode has a specific capacitance of 312 F/g in 1 mol/L H_2SO_4 electrolyte. Shi *et al.* activated anthracite coal using KOH and then synthesized a PC with the coexistence of micropores (63.6%), mesopores and macropores, an S_{BET} of 3550.7 m^2/g as well as a pore volume of 2.168 cm^3/g [21]. The specific capacitance reached 433 F/g (0.5 A/g), and the C_g retention rate was measured as 53.12% (50 A/g). However, since coal particles are characterized by a relatively small primary pore structure, it is difficult for the activators to access the inside of the particles, thus resulting in a small and insufficient contact for the activators and the coal particles. Consequently, due to inhomogeneously etch, the pore structure collapses, and excessive macroscopic pores generate. These synthesized PCs lead to poor electrolyte infiltration and limited surface utilization, which hinders the formation of an electric double layer, and thus reduces the capacitive and rate performances [23]. In addition, the ash in coal primarily originates from minerals, which mainly include metal oxides (*e.g.*, silicon and aluminum) [27], where strongly alkaline KOH can react with these metal oxides to generate soluble metal salts, which can be removed through subsequent acid treatment [28,29]. However, the de-ashing effect is significantly compromised, which arises from the insufficient contact between the KOH activator and the coal particles, as well as the difficulty for the acid liquid to enter the interior. The residual ash in the prepared PC will increase the resistance of the electrode and lead to an irreversible oxidation–reduction reaction, which reduces the electrochemical performances [3,28]. Accordingly, increasing the porosity of the coal precursor and its contact area with the activator and enhancing the permeability of the acid solution into the pore are of high significance to the activation effect and the de-ashing effect.

To overcome the above shortages, the design and synthesis of a coal-based carbon foam with high porosity and suitable surface chemical composition could be an advanced method to prepare hierarchical porous carbon (HPC), ensuring the sufficient contact for the activator and the electrolyte. Bituminous coal, benefiting from its unique structure and chemical composition, is always selected as the raw material to prepare porous carbon foam through pyrolysis foaming treatment. The formed carbon foam possesses abundant cells, high surface area and porosity, which should provide enough space for the attachment of the activator. In addition, the raw coal itself contains considerable heteroatoms, which can introduce a certain amount of surface functional groups. The appropriate functional groups could improve the wettability between aqueous electrolyte and carbon pores as well as introduce the pseudocapacitance, thus enhancing the energy storage of the HPC electrode. Thus, a green, scalable and efficient synthesis method of HPC from the coal precursor for supercapacitor application is urgently needed, which provides a new technique for high value-added utilization of the bituminous coal.

Here, two different coal-based carbon foams were employed to investigate the influence of hierarchical pore structure and surface chemical composition on the electrochemical properties of the HPC supercapacitor electrode. Scheme 1 gives a schematic diagram of the synthesis route of HPC by pyrolysis foaming and KOH activation, where the bituminous coal (RC) works as a raw precursor and a control (Table S1, Figs. S1 and S2 in Supporting information). During the pyrolysis process, volatile gas was released in the viscous metaplast to form bubbles, leading to the metaplast expanding foam. Further heating made the metaplast solidify with the bubble fixed inside to get the green carbon foam (NCF). The carbonized carbon foam (CCF) was achieved after subsequent

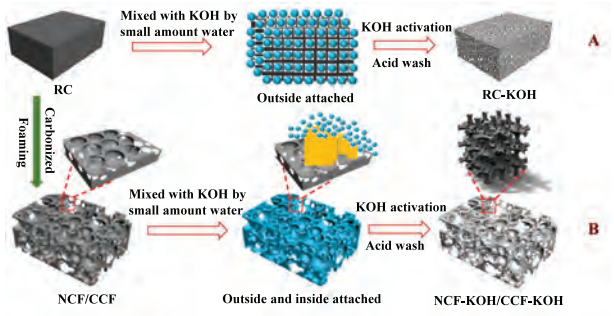

Scheme 1. Schematic diagram of the synthesis route of hierarchical porous carbon (HPC) from coal-based carbon foam (NCF/CCF, route B) with coal (RC, route A) as control.

high-temperature carbonization. The 3D interconnected hierarchical porous structures were then introduced into the carbon matrices of NCF and CCF by etching with the KOH activator. After subsequent acid washing, two HPCs, named NCF-KOH, CCF-KOH were obtained. For comparison, the RC was also directly activated under the above operating conditions with KOH, named RC-KOH. Compared with RC, the carbon matrices of NCF and CCF contained features of abundant cells, large surface area and high porosity with considerable attachment sites for the activator. And, the activator could penetrate deeply into the pores/cells to form outside and inside attached state, thus increasing the contact probability between the activator and the inner carbon skeleton atoms for efficient chemical activation. Thus, the NCF-KOH and CCF-KOH possessed interconnected hierarchical pore structures with abundant micropores that provide enough active surface for electrolyte adsorption, which was conducive to the formation of an electric double-layer capacitance. The optimal NCF-KOH with its hierarchical porous structure and an appropriate proportion of mesopores and micropores, promotes the permeation of electrolytes and the formation of ion diffusion channels. Moreover, the appropriate oxygen-containing functional groups could not only improve the wettability but also introduce a pseudocapacitance. With these features, NCF-KOH was endowed with a high specific capacitance of 487 F/g at 1 A/g, energy density of 10.34 Wh/kg at 249.6 W/kg, and outstanding long-cycling performance with the capacitance retention of 96% after 10,000 cycles at 5 A/g.

Raw coal has a flat surface morphology, a dense structure without pores and cracks (Fig. 1a and Fig. S3a in Supporting information). Through foaming, the cells of the carbon matrix in the synthesized NCF were cross-linked into a foam (cell size of 50–500 μm), which could be recognized as a typical carbon foam structure (Fig. 1b). Many small pores with relatively small sizes (<30 μm) were generated on the cell wall to form a 3D interconnected cell structure, and the cell wall was relatively smooth (Fig. S3b in Supporting information). After carbonization, CCF inherited the foam structure of NCF (Fig. 1c and Fig. S3c in Supporting information). After KOH activation of the carbon foam, the HCPs (NCF-KOH and CCF-KOH) retained the cell structure derived from NCF and CCF (Fig. S3d and g in Supporting information). The pore structure with different pore sizes and tight arrangement could be observed from the surface to the inside (*e.g.*, large pores of 200–500 nm) (Figs. 1e and f, Figs. S3e, f, h, i in Supporting information). This structure could contribute to the penetration of electrolyte ions [30]. For comparison, RC-KOH was synthesized (Fig. 1d and Fig. S3j in Supporting information) and presented an irregular block shape with a rough surface and a small number of holes (Fig. S3k and l in Supporting information). TEM images showed that abundant nanopores including micropores and mesopores were present in amorphous lattice fringes of HPCs (Figs. 1g–

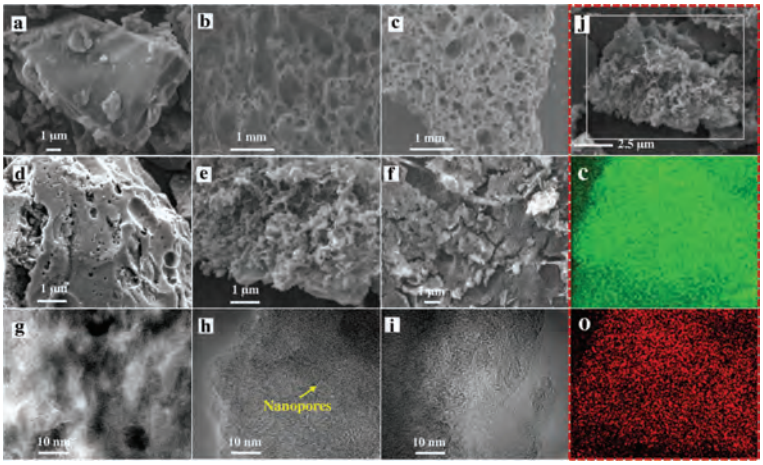

Fig. 1. Morphology characterization of hierarchical porous carbons (HPCs). SEM images of (a) RC, (b) NCF, (c) CCF, (d) RC-KOH, (e) NCF-KOH and (f) CCF-KOH. TEM images of (g) RC-KOH, (h) NCF-KOH, (i) CCF-KOH and (j) EDS mappings of C, O distributions in NCF-KOH.

i), in contrast to the graphite lattice fringes of RC-KOH [31]. The elementary mappings (Fig. 1j) showed that the surface of NCF-KOH largely consisted of C and O elements, coexisting in an overlapping manner and distributing throughout the sample.

S_{BET} and pore structure are both significant parameters for evaluating HPCs. All the HPCs show a type I/IV N_2 adsorption-desorption isotherm (Fig. S4a in Supporting information), indicating a similar micropore-dominated structure with a certain amount of mesopores and macropores (Fig. S4b in Supporting information) [20,23]. The micropores were mainly distributed between 0.4 nm and 2 nm, and the mesopores were distributed between 2 nm and 8 nm (Fig. S4b). The change rate of the pore volume of NCF-KOH between 0.7 nm and 2 nm was higher than those of CCF-KOH and RC-KOH. The S_{BET} and pore volume distribution of the HPCs (Fig. S4c,d and Table S2 in Supporting information) showed that NCF-KOH had a larger S_{BET} of 3472.41 m^2/g, total pore volume of 1.95 cm^3/g, and mesopore volume ratio (V_{mes}/V_{total}) of 57%, which were higher than those of CCF-KOH (1539.25 m^2/g, 0.94 cm^3/g and 49%) and RC-KOH (2725.12 m^2/g, 1.45 cm^3/g and 42%). The micropores created the surface for charge storage, mesopores provided the channel for ions transport, and the pores that were larger than 0.7 nm ($OH^- < K^+ \approx 0.4$ nm) could contribute to the formation of an electric double-layer and a passage of electrolyte ions in and out of the pores [32]. Therefore, sufficient S_{BET}, large pore volume and reasonable PSD laid the foundation for the excellent electrochemical performance of HPC electrode [2]. NCF-KOH exhibited the larger S_{BET}, more micropores in the range of 0.7–2.0 nm, bigger mesopores volume or V_{mes}/V_{total}, which indicates that it might exhibit the better electrochemical performances.

The microcrystalline structure of the HPCs was analyzed, and all the XRD spectra (Fig. 2a) exhibited two diffraction peaks at 25° and 43° corresponding to the (002) plane and (100) plane of graphitic phase, respectively [33]. The diffraction peaks at 25° tend to be broader and weaker, thus indicating that the etching effect of KOH could result in a decrease of the continuous sp^2–C stacking structure and an increase of the amorphous structure. Notably, NCF-KOH exhibited a more dispersive (002) diffraction peak than CCF-KOH, indicating that the KOH etching on NCF leads to the generation of more sp^3 hybrid carbon with amorphous phases. In addition, the XRD spectra of the three carbon matrices before activation showed some impurity peaks due to the existence of the ash minerals. KOH activation and acid washing treatment resulted in the disappearance of impurity peaks, indicating the significant reduction of the ash content in NCF-KOH and CCF-KOH to 0.35% and 0.63%, respectively (Table S3 in Supporting information). In contrast, 1.04% ash remained in RC-KOH (Table S3). This ash has different electric charges under the electric field, thus attracting the oppositely charged ions in the electrolyte solution and progressively forming agglomerations, which will block the ion diffusion channel and reduce the formation of the electric double-layer [28]. Correspondingly, the I_D/I_G values were significantly increased due to KOH activation from the Raman analysis (Fig. 2b), and the I_D/I_G of 0.88 for NCF-KOH was slightly higher than that of CCF-KOH (0.86), but significantly lower than that of RC-KOH. Therefore, the interconnected cell structure of carbon foam makes less defect density and the well-maintained carbon lattice of NCF-KOH and CCF-KOH. Moreover, I_D/I_G of the resultant HPCs was significantly lower than that of commercial activated carbon ($I_D/I_G = 1.92$, Norit (AC)), thus faciliating good electrical conductivity [34–36].

The XPS survey spectra (Fig. 2c) present the surface composition including heteroatoms of oxygen (O) in HPCs, which was found to play a key role in enhancing their electrochemical performance. Two main elements of C (282–294 eV) and O (527–539 eV) were identified on the surface. While the weak Si 2p, Al 2p, N 1s and S 2p signals indicated the presence of small amounts of Si, Al, N and S elements in the NCF, CCF and RC (Table S4 in Supporting information). After KOH activation, the Si 2p peak in NCF-KOH and CCF-KOH has disappeared, while a weak Si 2p peak remains in RC-KOH, which was related to the presence of a small amount of ash (1.04%, Table S3) in RC-KOH. The high-resolution spectrum of C 1s (Fig. 2d and Fig. S5 in Supporting information) showed four individual peaks at 284.5, 285.6, 287.5 and 289.7 eV, representing the sp^2–C/C=C, sp^3–C/C–C, C–O and C=O, respectively [9,37]. The high-resolution spectrum of O 1s (Fig. 2e and Fig. S5) contains three individual peaks at 530.3, 531–532, and 533–533.5 eV, representing the inorganic oxygen (IO), C=O and C–O, respectively [25,38]. After KOH activation, the sp^2–C decreased and the sp^3–C increased in HPCs (Table S5 in Supporting information), consistent with the change in the XRD peaks and the I_D/I_G from Raman analysis. NCF-KOH (O: 10.03%) and CCF-KOH (O: 11.98%, Table S4) showed similar oxygen-containing groups distributions, mainly C–O and C=O (*e.g.*, carbonyl C=O and carboxyl C=O) (Table S5, Fig. 2d and e). Likewise, the absorption vibration at 1620 cm^{-1} and 1000–1300 cm^{-1} in the FT-IR spectrum (Fig. 2f) of RC-KOH, NCF-KOH and CCF-KOH confirmed the existence of C=O and C–O [39]. The presence of C=O and C–O could not only improve the wettability and the full utilization of the exposed surface, but also introduce pseudocapacitance to enhance the capacity [40,41]. For RC-KOH, the high oxygen content (15.02%, Table S4) with considerable charged func-

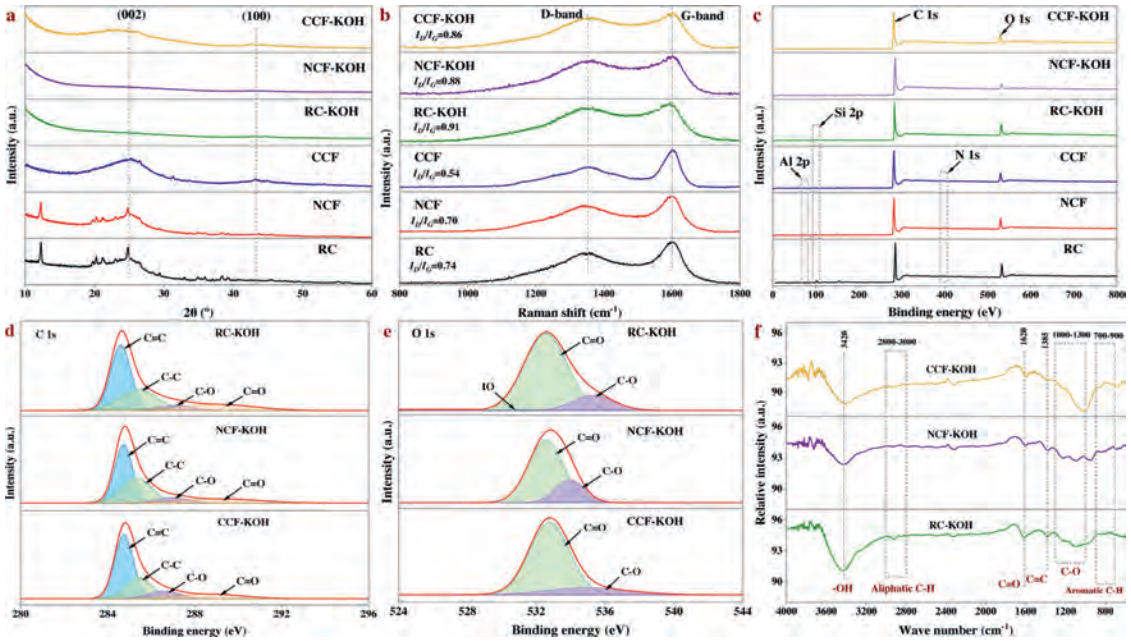

Fig. 2. Microcrystalline structure and surface chemical composition of HPC. (a) XRD patterns. (b) Raman spectra. (c) XPS survey spectra. (d) Deconvolution high-resolution C 1s XPS spectra of RC-KOH, NCF-KOH and CCF-KOH. (e) Deconvolution high-resolution O 1s XPS spectra of RC-KOH, NCF-KOH and CCF-KOH. (f) FT-IR spectra of RC-KOH, NCF-KOH and CCF-KOH.

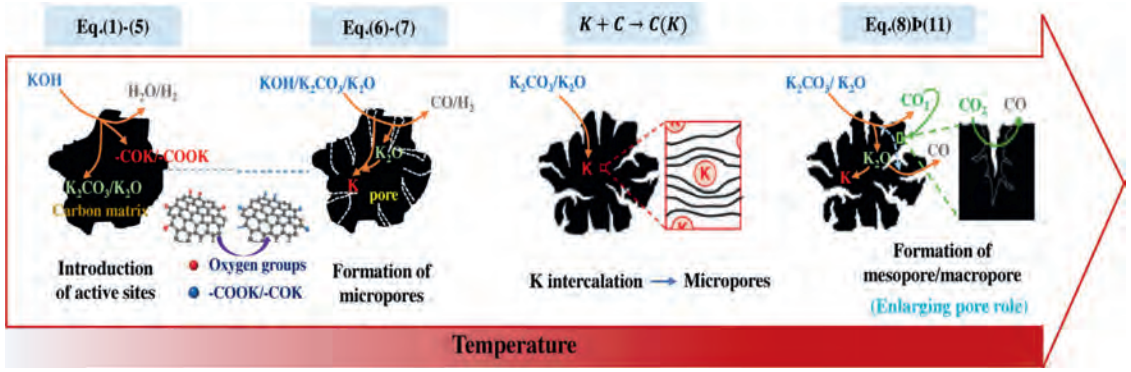

Fig. 3. Schematic illustration of the KOH activation process and mechanism for HPC.

tional groups was more prone to agglomeration, which blocks the formation of the electric double-layer [25,42]. Notably, there was no detectable IO in NCF-KOH and CCF-KOH, while, which could reduce the internal resistance of HPC as the electrode.

We further analyzed the KOH activation mechanism schematically shown in Fig. 3. The oxygen-containing functional groups and aliphatic side-chains on the surface of carbon matrix could react with KOH to introduce considerable active components, including –COK and –COOK (Eqs. 1–5), and to form active sites initiating the reaction of activator and carbon [43,44]. At the same time, the generated K_2CO_3, K_2O and residual KOH during this process were capable of reacting with the carbon atoms on the active site (Eqs. 6–11) [26,45]. This process would cause a strong etching effect on the carbon matrix, thus leading to the creation of considerable micropores in the carbon matrix. With the prolongation of reaction time, the micropore transformed to mesopore and then evolved into macropore (Fig. S6 in Supporting information). RC had the highest amount of oxygen-containing functional groups and aliphatic side-chain structures (Fig. S7 in Supporting information). Limited by the less pore structure, the high concentration of KOH present on the external surface of the RC led to an excessive and uneven etching of the surface carbon, thus facilitating the development of the generated micropores into mesopores, macropores, and then the evolution into large holes (Fig. 1d). The obtained RC-KOH had more defects and amorphous carbon. In contrast, the content of the aliphatic side-chain structure and the number of oxygen-containing functional groups in NCF were significantly reduced, corresponding to declining active sites. However, the three-dimensional (3D) interconnected cell structure, high porosity and large surface area would contribute to an increase in the permeability of KOH (Scheme 1). It could access the KOH activator inside the NCF, favoring to fully and uniformly etch the carbons on the cell walls. Accordingly, the carbon skeleton presented an interconnected porous structure composed of abundant micropores, mesopores and macropores (200–500 nm) and an amorphous structure. After carbonization at high temperature, active sites on CCF further decreased due to the reduction of the aliphatic side chain structure and oxygen-containing functional groups (Fig. S7). Moreover, CCF exhibited a dense carbon skeleton structure with fewer defect sites, which could increase the difficulty of the reaction between KOH and C. Fig. S6 and Table S6 (Supporting information) illustrated that both activation temperature and time could control the number and ratio of micropores and mesopores: either too low or too high temperature or time was not conducive to the im-

provement of S_{BET}. In addition, unlike the activation of RC, the KOH activator distributed over the whole surface of the carbon foam could fully undergo an alkali fusion reaction with ash (primarily SiO_2, Al_2O_3, Table S7 in Supporting information). It could not only remove the ash to generate more pores, but also consume more activators to prevent NCF and CCF from being over-activated. Notably, the HPCs still maintained the 3D skeleton structure of carbon foam with a hierarchical pore structure. The following acid treatment could easily contact the inside of HPCs to further remove the ash.

$$KOH + -COH \rightarrow -CO^{-}K^{+} + H_2O \uparrow \quad (1)$$

$$KOH + -COOH \rightarrow COOK + H_2O \uparrow \quad (2)$$

$$4KOH + -CH_2- \rightarrow K_2CO_3 + K_2O + 3H_2 \uparrow \quad (3)$$

$$KOH + -COOK \rightarrow K_2CO_3 + 1/2H_2 \uparrow \quad (4)$$

$$2KOH \rightarrow K_2O + H_2O \uparrow \quad (5)$$

$$K_2CO_3 + -CH_2- \rightarrow K_2O + 2CO \uparrow + H_2 \uparrow \quad (6)$$

$$K_2O + -CH_2- \rightarrow 2K + CO \uparrow + H_2 \uparrow \quad (7)$$

$$1/2K_2CO_3 + C \rightarrow K + 3/2CO \uparrow \quad (8)$$

$$K_2CO_3 \rightarrow K_2O + CO_2 \quad (9)$$

$$K_2O + C \rightarrow 2K + CO \uparrow \quad (10)$$

$$C + CO_2 \rightarrow 2CO \quad (11)$$

The electrochemical performance of HPC as supercapacitor electrode was firstly investigated in a three-electrode configuration with a potential window from −1 V to 0 V using 6 mo/L KOH as the aqueous electrolyte. The CV curves at 10 mV/s (Fig. 4a) and GCD curves at 1 A/g (Fig. 4b) present the near rectangle and isosceles triangle shapes, respectively, indicating the high electrical double-layer capacitance behavior [46,47]. The weak redox peaks close to −0.6 V *vs.* Hg/HgO in the CV curves and the slight bending of the GCD curves could belong to the additional pseudocapacitive behavior stemming from the heteroatom oxygen on the surface [35,48], which was detected using XPS spectra (Figs. 2c–e, Tables S4 and S5). When the scan rate was increased (5–100 mV/s), all the CV curves of NCF-KOH and CCF-KOH maintained quasi-rectangular shape (Fig. 4c and Fig. S8a in Supporting information), which belonged to the EDLC capacitance characteristics, thus implying excellent energy storage performance. In comparison, for RC-KOH, the symmetry of the CV curves reduced and changed from rectangular to elliptical when the scan rate was higher than 50 mV/s in Fig. S8b (Supporting information). Increasing the current density, ranging from 1 A/g to 50 A/g, the GCD curves of NCF-KOH and CCF-KOH maintained isosceles triangle shapes without obvious voltage drop (*IR*) (Fig. 4d and Fig. S8c in Supporting information), indicating the highly reversible charge-discharge electrochemical performance. The slight *IR* of RC-KOH at higher current densities in Fig. S8d (Supporting information) corresponded to the distortion in the CV curves. The specific capacitance (C_g) was determined from GCD curves based on Eq. S1 (Supporting information), presented in Figs. 4e and f. NCF-KOH displayed a high C_g of 487 F/g at 1 A/g, which was 2.0 and 2.3 times higher than CCF-KOH (241 F/g) and RC-KOH (212 F/g), respectively. As the rate current increased to 50 A/g, the C_g remained 400 F/g, 2.0 and 2.9 times larger than that of CCF-KOH (196 F/g) and RC-KOH (140 F/g). Under the identical condition shown in Table S8 (Supporting information), NCF-KOH presents comparable or even higher C_g than these carbon materials previously reported, thus revealing its promising application in high-performance supercapacitors.

The electrochemical impedance (EIS) and its corresponding equivalent circuit diagrams were used to investigate the electrochemical kinetic process. From the Nyquist plots (Fig. 4g), the tails in the low frequency region are nearly vertical toward the real axis, indicating an excellent capacitive behavior of the two HPCs [22,40]. At high frequencies, the intercept of the EIS curve on the X-axis represents the intrinsic resistance (R_e) of the electrode material [12,49]. The R_e of 0.7 Ω for NCF-KOH was about 142.8% for CCF-KOH (0.49 Ω) and 46.7% for RC-KOH (1.50 Ω), respectively. And, NCF-KOH showed a smaller diameter of the semicircle in the high frequency region, denoting a charge-transfer resistance of 0.81 Ω, which was 44.5 and 28.2% of CCF-KOH (1.82 Ω) and RC-KOH (3.35 Ω), respectively. Moreover, the relaxation time constant (τ_0) of 0.485 s for NCF-KOH was also lower than that of CCF-KOH (0.616 s) and RC-KOH (1.114 s) from the Bode plots (Fig. 4h) [50–53], indicating the robust electrochemical charge-discharge kinetics of NCF-KOH, mainly originated from fast ion transport in interconnected porous structure with high V_{mes}/V_{total} ratio.

To gain insights into the energy storage of HPC in practical applications, symmetrical supercapacitors using NCF-KOH as the electrodes were assembled with 6 mol/L KOH electrolyte to investigate the electrochemical properties (Fig. 5 and Fig. S9 in Supporting information). As indicated by Figs. 5a and b, NCF-KOH exhibited ideal EDLCs behaviors. And the shape of the CV curve for NCF-KOH was unchanged even at the scan rate increasing to 500 mV/s (Fig. 5c), confirming the fast charge-discharge behavior in the assembled symmetrical supercapacitor. Furthermore, the charge-discharge curves were not aligned in Fig. 5d, indicating that a pseudocapacitor behavior was induced by surface oxygen. The GCD curves of NCF-KOH at different current densities had a tiny *IR* drop (Fig. S10 in Supporting information), indicating a low intrinsic resistance (R_e, Fig. 4g) and large power delivery. Fig. 5e presents the C_s of NCF-KOH at the current densities ranging from 0.5 to 50 A/g according to Eq. S2 (Supporting information). The C_s of NCF-KOH decreased with the increase of current density because of the existence of electrical resistance and the generation of concentration polarization. The C_s sustained from 299 F/g to 220 F/g during the current density increasing from 0.5 to 50 A/g, a capacitance retention of 73.4%, which was better than that of CCF-KOH (70.8%), RC-KOH (66.7%), and other carbon materials reported under the same conditions [54,55]. In addition, Fig. S11 (Supporting information) gives the GCD curves of NCF-KOH at 0.1 and 0.2 A/g, where C_s of NCF-KOH was 371 F/g at a current density of 0.1 A/g (Table S9 in Supporting information). The energy density (*E*, Eq. S3 in Supporting information) and power density (*P*, Eq. S4 in Supporting information) are crucial parameters to evaluate the electrochemical performance of supercapacitor [51,56]. The NCF-KOH exhibited a maximum *E* of 12.9 Wh/kg at the *P* of 50.0 W/kg (0.1 A/g), while *E* remained 10.34 Wh/kg at *P* of 249.6 W/kg (0.5 A/g). Moreover, *E* was still 5.76 Wh/kg (50 A/g), when *P* reached 21,753.2 W/kg (Fig. 5f), which revealed that NCF-KOH maintained excellent energy storage capability under a large current density. Compared with reported carbon electrodes [57–60], NCF-KOH exhibited a competitive *E*, thus showing the potential of being extensively used as a high-performance and low-cost electrode for supercapacitors applications. As shown in Fig. 5g, the assembled symmetrical supercapacitor presents excellent electrochemical stability upon 10,000 cycles at 5 A/g with a coulombic efficiency (η, Eq. S5 in Supporting

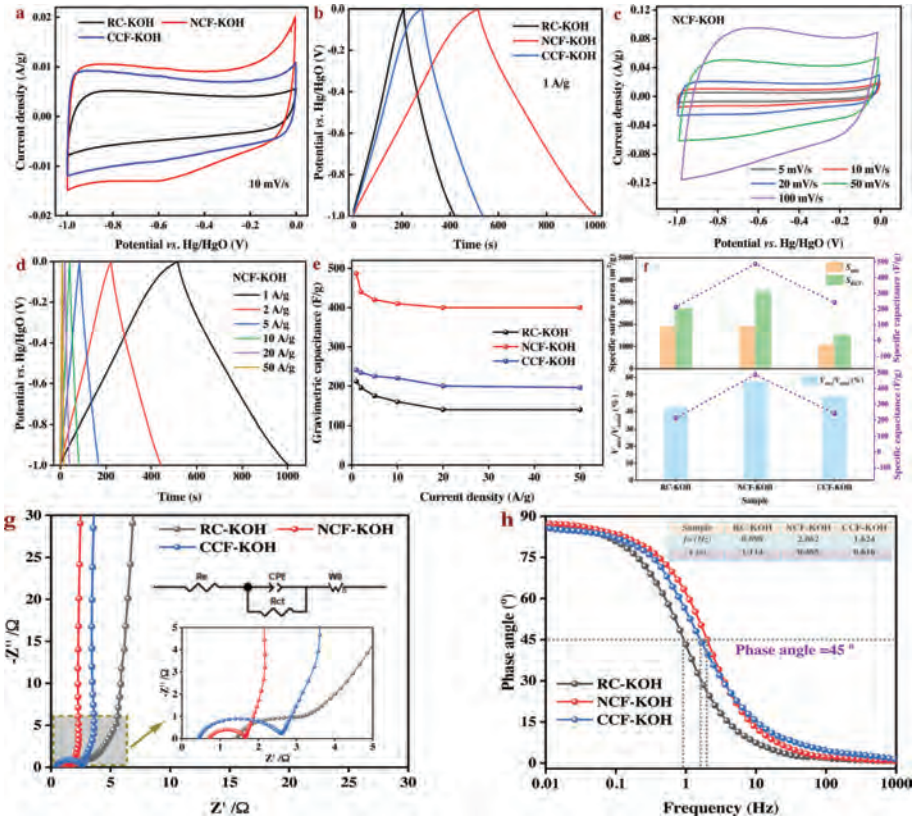

Fig. 4. Electrochemical performances of HPC as supercapacitor electrode in the three-electrode configuration. (a) CV curves at a scan rate of 10 mV/s. (b) GCD curves at a current density of 1 A/g. (c) CV curves of NCF-KOH at scan rates ranging from 5 mV/s to 100 mV/s. (d) GCD curves of NCF-KOH at current densities from 1 A/g to 50 A/g. (e) C_g at variable current densities. (f) Correlation of C_g with S_{BET} and V_{meso}/V_{total}. (g) Nyquist plots, inset: equivalent circuit diagrams. (h) Bode plots.

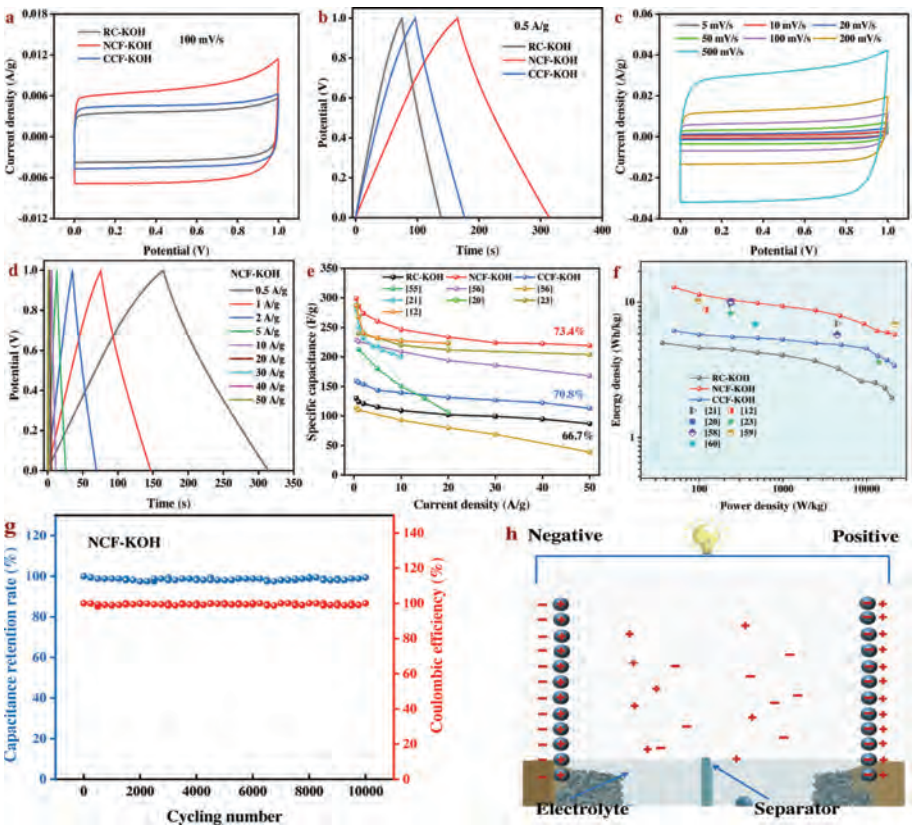

Fig. 5. Electrochemical performance of HPC as supercapacitor electrode in a symmetrical configuration. (a) CV curves at 100 mV/s. (b) GCD curves at 0.5 A/g. (c) CV curves at scan rate in the range of 5–500 mV/s for NCF-KOH. (d) GCD curves at current density in the range of 0.5–50 A/g for NCF-KOH. (e) Rate capability. (f) Ragone plots. (g) Cycling stability at 5 A/g. (h) Schematic illustration of HPC in a symmetrical configuration.

information) of 98% and the capacitance retention of 96%, due to the 3D interconnected hierarchical porous structure and the structural stability (Fig. S12 in Supporting information).

The energy storage working mechanism of NCF-KOH//NCF-KOH with KOH solution as the electrolyte is mainly through the adsorption/desorption of OH^-/K^+ ions in the electric double-layer formed at the interface between the electrolyte and NCF-KOH electrode to store charges (Fig. 5h). Thus, the capacitive performance is largely dependent on the accessible S_{BET}, interconnected hierarchical pores and carbon skeleton, providing high ion diffusion and electrical conductivity capability of NCF-KOH. The interconnected hierarchical porous structure with large accessible surface areas and an appropriate amount of oxygen-containing functional groups enable the 3D ionic channel for the penetration of electrolytes and ions migration.

In summary, a novel interconnected hierarchical porous carbon from raw coal was designed to work as an advanced supercapacitor electrode material. The interconnected hierarchical pore structure with large accessible surface and surface oxygen-containing functional groups constructed the 3D ionic channel and electrical conductivity pathway for electric double-layer capacitance towards high capacity, high energy and high power supercapacitor. This pyrolysis foaming and KOH activation technique to convert coal into advanced carbon materials provide a prospective direction for green and high value-added utilization of the coal.

Declaration of competing interest

The authors declare no competing financial interests.

Acknowledgments

The authors gratefully acknowledge the financial support of National Natural Science Foundation of China (Nos. U1910201, 21878208, 21961024), Shanxi Province Science Foundation for Key Program (No. 201901D111001(ZD)), Inner Mongolia Natural Science Foundation (No. 2018JQ05), Inner Mongolia Autonomous Region Science & Technology Planning Project for Applied Technology Research and Development (No. 2019GG261).

Supplementary materials

Supplementary material associated with this article can be found, in the online version, at doi:10.1016/j.cclet.2022.03.037.

References

[1] M. Sevilla, R. Mokaya, Energy. Environ. Sci. 7 (2014) 1250–1280.
[2] A. Borenstein, O. Hanna, R. Attias, et al., J. Mater. Chem. A 5 (2017) 12653–12672.
[3] L.L. Zhang, X.S. Zhao, Chem. Soc. Rev. 38 (2009) 2520–2531.
[4] S. Peng, L. Li, H.B. Wu, S. Madhavi, X.W.D. Lou, Adv. Energy Mater. 5 (2015) 1401172.
[5] J. Yan, Q. Wang, T. Wei, Z. Fan, Adv. Energy Mater. 4 (2014) 1300816.
[6] D.P. Chatterjee, A.K. Nandi, J. Mater. Chem. A 9 (2021) 15880–15918.
[7] L. Li, S. Peng, H.Y. Chen, et al., Nano Energy 19 (2016) 307–317.
[8] L. Li, S. Peng, H.B. Wu, et al., Adv. Energy Mater. 5 (2015) 1500753.
[9] H. Wei, H. Wang, A. Li, et al., J. Alloy. Compd. 820 (2020) 153111.
[10] X. Chen, R. Paul, L. Dai, Natl. Sci. Rev. 4 (2017) 453–489.
[11] M.L. Wang, T.Y. Zhang, M.Z. Cui, et al., Chin. Chem. Lett. 32 (2021) 1111–1116.
[12] G. Han, J. Jia, Q. Liu, et al., Carbon 186 (2022) 380–390.
[13] A. González, E. Goikolea, J.A. Barrena, et al., Renew. Sustain. Energy Rev. 58 (2016) 1189–1206.
[14] Q. Fang, W. Zhang, X.H. Chen, Y.J. Zhang, M. Hu, Chin. Chem. Lett. 31 (2020) 303–306.
[15] H. Lu, Q. Li, J. Guo, et al., Appl. Surf. Sci. 427 (2018) 992–999.
[16] G.C. Ping, L. Miao, A. Awati, et al., Chin. Chem. Lett. 32 (2021) 3811–3816.
[17] K.K. Li, G.Y. Liu, L.S. Zheng, et al., New Carbon Mater. 36 (2021) 133–154.
[18] X. Ma, X. Dong, Y. Fan, Energy Fuel 32 (2018) 3097–3107.
[19] L. Xu, H. Liu, Y. Jin, et al., Fuel 137 (2014) 164–171.
[20] D. Dong, Y. Zhang, Y. Xiao, et al., J. Colloid Interface Sci. 580 (2020) 77–87.
[21] M. Shi, Y. Xin, X. Chen, et al., J. Alloy. Compd. 859 (2021) 157856.
[22] X.M. Yue, Z.Y. An, M. Ye, et al., Molecules 24 (2019) 3588.
[23] Y. Jiang, Z. Jiang, M. Shi, et al., Carbon 182 (2021) 559–563.
[24] J. Chmiola, G. Yushin, R. Dash, Y. Gogotsi, J. Power Sources 158 (2006) 765–772.
[25] X. Cai, Q. Ren, W. Sun, F. Yang, Int. J. Energy Res. 45 (2021) 21414–21434.
[26] K. Kierzek, E. Frackowiak, G. Lota, G. Gryglewicz, J. Machnikowski, Electrochim. Acta 49 (2004) 515–523.
[27] H. Jin, X.M. Wang, Z.G. Gu, Mater. Focus 2 (2013) 105–112.
[28] J. Zhang, L. Jin, J. Cheng, H. Hu, Carbon 55 (2013) 221–232.
[29] T.H. Liou, S.J. Wu, J. Hazard. Mater. 171 (2009) 693–703.
[30] J. Balach, M.M. Bruno, N.G. Cotella, et al., J. Power Sources 199 (2012) 386–394.
[31] S. Ghosh, R. Sarathi, S. Ramaprabhu, J. Colloid Interface Sci. 539 (2019) 245–256.
[32] M. Inagaki, H. Konno, O. Tanaike, J. Power Sources 195 (2010) 7880–7903.
[33] Y. Xiao, C. Long, M.T. Zheng, et al., Chin. Chem. Lett. 25 (2014) 865–868.
[34] S. Maruyama, T. Fukutsuka, K. Miyazaki, T. Abe, Electrochim. Acta 265 (2018) 41–46.
[35] L. Hou, W. Yang, Y. Li, et al., Chem. Eng. J. 417 (2021) 129289.
[36] H.L. Wang, Z.W. Xu, A. Kohandehghan, et al., ACS Nano 7 (2013) 5131–5141.
[37] E. Raymundo-Piñero, F. Leroux, F. Béguin, Adv. Mater. 18 (2006) 1877–1882.
[38] P. Li, C.N. Feng, H.P. Li, X.L. Zhang, X.C. Zheng, J. Alloy. Compd. 851 (2021) 156922.
[39] K.C. Bedin, A.C. Martins, A.L. Cazetta, O. Pezoti, V.C. Almeida, Chem. Eng. J. 286 (2016) 476–484.
[40] Y. Zhan, H. Zhou, F. Guo, et al., J. Energy Storage 34 (2021) 102180.
[41] B. Fang, Y.Z. Wei, M. Kumagai, J. Power Sources 155 (2006) 487–491.
[42] C. Zhang, D. Long, B. Xing, et al., Electrochem. Commun. 10 (2008) 1809–1811.
[43] P. Ehrburger, A. Addoun, F. Addoun, J.B. Donnet, Fuel 65 (1986) 1447–1449.
[44] M.A. Lillo-Ródenas, D. Cazorla-Amorós, A. Linares-Solano, Carbon 41 (2003) 267–275.
[45] M. Sevilla, N. Diez, A.B. Fuertes, ChemSusChem 14 (2021) 94–117.
[46] X. He, P. Ling, J. Qiu, et al., J. Power Sources 240 (2013) 109–113.
[47] D. Wang, G. Fang, T. Xue, J. Ma, G. Geng, J. Power Sources 307 (2016) 401–409.
[48] Y. Shu, Q. Bai, G. Fu, et al., Carbohydr. Polym. 227 (2020) 115346.
[49] H. Peng, B. Yao, X. Wei, et al., Adv. Energy Mater. 9 (2019) 1803665.
[50] J. Zhao, H. Lai, Z. Lyu, et al., Adv. Mater. 27 (2015) 3541–3545.
[51] K. Sun, S. Yu, Z. Hu, et al., Electrochim. Acta 231 (2017) 417–428.
[52] T. Lin, I. Chen, F. Liu, et al., Science 350 (2015) 1508–1513.
[53] C. Ma, Y. Song, J. Shi, et al., Carbon 51 (2013) 290–300.
[54] S. Yaglikci, Y. Gokce, E. Yagmur, A. Banford, Z. Aktas, Surf. Interfaces 22 (2021) 100899.
[55] Z. Li, A. Cheng, W. Zhong, et al., Microporous and Mesoporous Mater. 306 (2020) 110440.
[56] J. Li, W. Liu, D. Xiao, X. Wang, Appl. Surf. Sci. 416 (2017) 918–924.
[57] Y. Wang, Y. Liu, D. Wang, et al., Appl. Surf. Sci. 506 (2020) 145014.
[58] Y. Gong, D. Li, Q. Fu, Y. Zhang, C. Pan, ACS Appl. Energy Mater. 3 (2020) 1585–1592.
[59] X. Zhang, B. Sun, X. Fan, et al., Fuel 311 (2021) 122552.
[60] G.A. Yakaboylu, C. Jiang, T. Yumak, et al., Renew. Energy 163 (2021) 276–287.